Analysis of cracked shear deformable plates by an effective meshfree plate formulation

Satoyuki Tanaka[a], Hirotaka Suzuki[a], Shota Sadamoto[a],
Michiya Imachi[a], Tinh Quoc Bui[b]

[a] *Graduate School of Engineering, Hiroshima University, Japan,*
e-mail: satoyuki@hiroshima-u.ac.jp, m140825@hiroshima-u.ac.jp,
shota.sadamoto@gmail.com, m155994@hiroshima-u.ac.jp
[b] *Department of Mechanical and Environmental Informatics,*
Tokyo Institute of Technology, Japan, e-mail: tinh.buiquoc@gmail.com

---

Abstract

A novel technique to evaluate the path-independent integral using nodal integration is developed for cracked plate problems. The formulation is based on the Mindlin-Reissner plate theory, and the reproducing kernel is used as a meshfree interpolant. A visibility criterion, diffraction method, and enriched basis are included. To integrate the stiffness matrix, the stabilized conforming nodal integration and the sub-domain conforming integration are adopted. A moment intensity factor is also evaluated employing the J-integral based on the nodal integration. Convergence and numerical results derived from regular and irregular discretizations, node density, and other aspect ratios are analyzed.

Keywords: Fracture; Meshfree methods; Mindlin-Reissner plates;
J-integral; Stabilized conforming nodal integration.

---

1. Introduction

Hull structures of ships and offshore structures are composed of plates. To ensure structural safety and reliability in practical design of the plate structures, durability assessments against cracking is important. Fracture mechanics is one of the techniques in this assessment. Researchers have performed fracture mechanics and failure analyses for marine structures [1-4].

Preprint submitted to Engineering Fracture Mechanics *June 22, 2015*

Generally, crack analyses and evaluation of the stress intensity factors (SIFs) have been performed based on three-dimensional (3D) continuum theory [5]. The plate structures are deformed out of the plane under different loading conditions. Fracture mechanics formulated by a plate theory is well suited for describing fracturing of cracked thin-plate structures. When performing fracture mechanics evaluations based on the plate theory formulation, the mathematical representation of deformation, strain, and stress around the crack tip are different from those of the 3D continuum theory. A crack analysis in plates and shells, and collections of SIF solutions are summarized in [6]. Zhender and Viz [7] reviewed fracture mechanics of a cracked plate including Kirchhoff and Mindlin-Reissner plate formulations. To date, crack analysis based on plate theory is rather rare compared with that using 3D continuum theory. Further investigations are therefore needed, *e.g.*, cracked plate modeling, evaluation of the fracture mechanics parameters, and the crack propagation simulations. In this paper, we analyze cracked width plates using a novel meshfree plate formulation in terms of the Mindlin-Reissner shear deformable theory and stabilized conforming nodal integration.

In solving plate bending problems employing a standard finite element (FE) formulation, a special technique is needed to overcome the shear locking problem. A recently developed numerical method, the meshfree method, has the potential to avoid the locking problem because continuous functions can be adopted in the approximation of the deflection and rotation components. To date, various meshfree methods have been proposed, *e.g.*, the element free Galerkin method [8], the reproducing kernel particle method [9,10], the meshless local Petrov-Galerkin method [11], and the moving Kriging interpolation method [12,13]. An interesting overview and recent developments of the meshfree methods can be found in [14]. The moving least squares approximation or the reproducing kernel (RK) approximation are frequently employed to generate the meshfree interpolants. The function and its derivative are smooth and continuous. In this study, the Mindlin-Reissner plate formulation proposed by Wang and Chen [15,16] and the RK approximation [9] are adopted, and the stabilized conforming nodal integration (SCNI) [17] is employed to integrate the stiffness matrix. The formulation and discretization assumes a locking-free property by imposing the so-called Kirchhoff mode reproducing condition (KMRC). In our previous study, large deflection analyses of a stiffened plate structure employing the meshfree plate formulation were presented in [18].

In recent years, several computer methods have been proposed to solve cracked bending plate problems. The X-FEM with enrichment functions [19] was introduced into the Mindlin-Reissner plate theory [20-22] and Kirchhoff plate theory [23]. Dirgantara and Aliabadi solved the problems for cracked shells [24] and thin-plates [25] using the dual boundary element method [26]. Fracture in thin-shells was treated with overlapping paired elements in [27]. Nonlinear dynamic fracturing in thin shells was analyzed employing enriched particles and local partition of the unity approach in [28]. The phantom-node method [29] was applied in the analysis of cracks in shell models in [30]. Bhardwaj *et al.* [31] presented a numerical simulation of a functionally graded cracked plated based on first order shear deformation theory under different boundary and loading conditions using the extended isogeometric analysis [32].

In this study, a cracked plate is analyzed employing the meshfree Mindlin-Reissner plate formulation. To model a cracked plate, various schemes including a visibility criterion, the diffraction method, and an enriched basis are used. The techniques were introduced in the meshfree analysis for two-dimensional (2D) in-plane crack problems [33-36]. In addition, the SCNI is employed to numerically integrate the stiffness matrix. Sub-domain stabilized conforming integration (SSCI) [37-38] is also applied to accurately represent the displacement discontinuity across the crack segment. To evaluate the moment intensity factor, a path-independent integral (J-integral) formulated by the plate theory [39,40] is used. The problem domain is discretized on SCNI and SSCI, and the J-value is estimated by summing the physical quantities using nodal integration. In this way, not only the smoothed values are used but also the computational efficiency is enhanced in the path-independent integral. Although the meshfree crack modeling was applied to solve 2D in-plane problems, as far as we know, the crack modeling employing the RKs for the shear deformable plate problems, and the J-integral evaluations with SCNI and SSCI has not yet been reported. Therefore, we present in this paper a novel meshless formulation of crack modeling for shear deformable plates, evaluating the J-integral with the aid of the SCNI. The method is free of shear-locking, no FE meshes, highly suitable for crack modeling and high accuracy. Several numerical examples are given to demonstrate the validity of the proposed approach.

The paper is structured as follows: A mathematical formulation for the shear deformable plate and the discretization employing the meshfree method are presented in Section 2. The crack modeling and the J-integral evaluation for the plate bending problems are discussed in Section 3. Section 4 demonstrates several numerical examples for the cracked plates to validate the proposed approach. Some concluding remarks arising from the study are given in the last section.

2. Meshfree formulation for cracked shear deformable plates

2.1. Plate bending problem formulated by Mindlin-Reissner plate theory

As depicted in Fig.1, we consider a shear deformable plate containing a through-thickness crack denoted by Γ_c. The analysis domain is Ω, and is bounded by Γ. The plate thickness is t. The x_1-x_2 plane is assumed to be located at the mid-surface of the plate. The x_3-direction is defined perpendicular to the mid-plane. A shear deformable plate without a crack is however formulated first.

The plate formulation has three components w, θ_1 and θ_2 in which. w is the deflection and θ_1 and θ_2 are rotation angles about the axial directions x_1 and x_2, respectively. Throughout the study, the material is assumed to be a linear isotropic elastic medium subjected to small strains and rotations.

The plate deformation $\boldsymbol{u}(\boldsymbol{x})$ can be written in terms of the deflection and rotation components as follows:

$$\boldsymbol{u}(\boldsymbol{x}) = \left\{ \begin{array}{c} u_1(\boldsymbol{x}) \\ u_2(\boldsymbol{x}) \\ u_3(\boldsymbol{x}) \end{array} \right\} = \left\{ \begin{array}{c} -z\theta_1(\boldsymbol{x}) \\ -z\theta_2(\boldsymbol{x}) \\ w(\boldsymbol{x}) \end{array} \right\}, \tag{1}$$

where $u_i(\boldsymbol{x})$ (i= 1, 2, 3) are the displacements along the x_i-axis. z ($|z| \leq t/2$) represents the plate thickness direction.

The strains $\boldsymbol{\varepsilon}^b$=$\{\varepsilon_{11} \quad \varepsilon_{22} \quad \varepsilon_{12}\}^T$ and $\boldsymbol{\varepsilon}^s$=$\{\varepsilon_{23} \quad \varepsilon_{31}\}^T$ are written in the Mindlin-Reissner plate formulation as

$$\boldsymbol{\epsilon}^b = -z\boldsymbol{\kappa} = -z \left\{ \begin{array}{c} \frac{\partial\theta_1}{\partial x_1} \\ \frac{\partial\theta_2}{\partial x_2} \\ \frac{\partial\theta_2}{\partial x_1} + \frac{\partial\theta_1}{\partial x_2} \end{array} \right\}, \quad \boldsymbol{\epsilon}^s = \boldsymbol{\gamma} = \left\{ \begin{array}{c} \frac{\partial w}{\partial x_1} - \theta_1 \\ \frac{\partial w}{\partial x_2} - \theta_2 \end{array} \right\}, \tag{2}$$

where $\boldsymbol{\kappa} = \{\kappa_{11}\ \ \kappa_{22}\ \ 2\kappa_{12}\}^T$ is the curvature and $\boldsymbol{\gamma} = \{\gamma_1\ \ \gamma_2\}^T$ is the shear strain. The displacement $\boldsymbol{u}(\boldsymbol{x})$, curvature $\boldsymbol{\kappa}$ and shear strain components $\boldsymbol{\gamma}$ are approximated by RKs.

When employing the Galerkin-based discretization, the virtual work principle for the shear deformable plate is expressibled as:

$$\int_{\Omega}(z^2\delta\boldsymbol{\kappa}^T\boldsymbol{D}^b\boldsymbol{\kappa} + \delta\boldsymbol{\gamma}^T\boldsymbol{D}^s\boldsymbol{\gamma})d\Omega - \delta W = 0, \tag{3}$$

$$\delta W = \int_{\Omega}\delta w p d\Omega - \int_{\Gamma^h}\delta\theta_n M_{nn} d\Gamma, \tag{4}$$

$$u_i(\boldsymbol{x}) = \bar{u}_i \quad on \quad \Gamma^g, \tag{5}$$

where $\delta\boldsymbol{\kappa}$, $\delta\boldsymbol{\gamma}$, δw and $\delta\theta_n$ are the variations corresponding to curvature, shear strain, deflection and rotation, respectively. p and M_{nn} are the distributed stress on Ω and moments on Γ^h. The deflection and rotations are prescribed by $\bar{u}_i$ on Γ^g. $\boldsymbol{D}^b$ and $\boldsymbol{D}^s$ are matrices of elastic constants in terms of the bending and shear components. These elastic matrices are represented as

$$\boldsymbol{D}^b = \frac{E}{(1-\nu^2)}\left[\begin{array}{ccc} 1 & \nu & 0 \\ \nu & 1 & 0 \\ 0 & 0 & \frac{1-\nu}{2} \end{array}\right], \quad \boldsymbol{D}^s = kG\left[\begin{array}{cc} 1 & 0 \\ 0 & 1 \end{array}\right], \tag{6}$$

where E, ν and G $(= E/2(1+\nu))$ are Young's modulus, Poisson's ratio, and the shear modulus, respectively. The shear correction factor is set to k=$\pi^2/12$. The moment and shear force vectors $\boldsymbol{M}$ and $\boldsymbol{Q}$ have the following form

$$\boldsymbol{M} = \left\{\begin{array}{c} M_{11} \\ M_{22} \\ M_{12} \end{array}\right\} = \int_{-t/2}^{t/2} -z^2\boldsymbol{D}^b\boldsymbol{\kappa}dz, \quad \boldsymbol{Q} = \left\{\begin{array}{c} Q_1 \\ Q_2 \end{array}\right\} = \int_{-t/2}^{t/2} -\boldsymbol{D}^s\boldsymbol{\gamma}dz. \tag{7}$$

2.2. RK approximation

The mid-surface of the plate is discretized by a set of scattered nodes, as depicted in Fig.1. A position vector of node I is $\boldsymbol{x}_I$ $(I = 1, \cdots, \mathrm{NP})$. Hereafter, all the deflection $w(\boldsymbol{x})$, and rotation components $\theta_1(\boldsymbol{x})$ and $\theta_2(\boldsymbol{x})$ are rewritten as $d_i(\boldsymbol{x})$ $(i = 1, 2, 3)$. The components are approximated by the RKs through the following relation

$$d_i^h(\boldsymbol{x}) = \sum_{I=1}^{\mathrm{NP}}\Psi_I(\boldsymbol{x})d_{iI}, \tag{8}$$

where $\Psi_I(\boldsymbol{x})$ are the RKs of node I, and d_{iI} are their coefficients. The RKs are constructed as the sum of the original kernels and satisfy a so-called consistency condition [9]

$$\Psi_I(\boldsymbol{x}) = \boldsymbol{H}^T(\boldsymbol{x}_I - \boldsymbol{x})\boldsymbol{b}(\boldsymbol{x})\phi_{aI}(\boldsymbol{x}_I - \boldsymbol{x}), \tag{9}$$

where $\boldsymbol{H}(\boldsymbol{x}_I - \boldsymbol{x})$ is a basis vector, and $\boldsymbol{b}(\boldsymbol{x})$ a coefficient vector. $\phi_{aI}(\boldsymbol{x})$ is an original kernel, and the following cubic spline function is adopted;

$$\phi_{aI}(\boldsymbol{x}_I - \boldsymbol{x}, h) = \frac{10}{7\pi h^2}\left\{\begin{array}{cc} 1 - \frac{3}{2}s^2 + \frac{3}{4}s^3 & (0 \le s \le 1) \\ \frac{1}{4}(2-s)^3 & (1 \le s \le 2) \\ 0 & (2 \le s) \end{array}\right. , \tag{10}$$

where $s(=||\boldsymbol{x}_I - \boldsymbol{x}||/h)$ is the normalized distance from the center of the kernel, and h is a parameter that determines the function support.

The plate deformation $\boldsymbol{u}(\boldsymbol{x})$ of Eq.(1) are approximated by the RKs, and written in matrix form as

$$\boldsymbol{u}^h(\boldsymbol{x}) = \sum_{I=1}^{\mathrm{NP}} \boldsymbol{N}_I \boldsymbol{d}_I, \quad \boldsymbol{N}_I = \left[\begin{array}{ccc} 0 & -z\Psi_I & 0 \\ 0 & 0 & -z\Psi_I \\ \Psi_I & 0 & 0 \end{array}\right], \tag{11}$$

where $\boldsymbol{u}^h(\boldsymbol{x})$=$\{u_1^h(\boldsymbol{x}), u_2^h(\boldsymbol{x}), u_3^h(\boldsymbol{x})\}^T$ denotes the approximate value vector for the deflection and rotations at position $\boldsymbol{x}$. $\boldsymbol{d}_I$=$\{d_{1I}, d_{2I}, d_{3I}\}^T$ is a vector of coefficients. $\boldsymbol{N}_I$ is matrix composed of the RKs.

In a similar manner, the curvature $\boldsymbol{\kappa}$ and the shear strain $\boldsymbol{\gamma}$ are approximated as

$$\boldsymbol{\kappa}^h = \left\{\begin{array}{c} \kappa_{11}^h \\ \kappa_{22}^h \\ 2\kappa_{12}^h \end{array}\right\} = \sum_{I=1}^{\mathrm{NP}} \boldsymbol{B}_I^b \boldsymbol{d}_I, \quad \boldsymbol{\gamma}^h = \left\{\begin{array}{c} \gamma_1^h \\ \gamma_2^h \end{array}\right\} = \sum_{I=1}^{\mathrm{NP}} \boldsymbol{B}_I^s \boldsymbol{d}_I. \tag{12}$$

The displacement-strain matrices $\boldsymbol{B}_I^b$ and $\boldsymbol{B}_I^s$ for the bending and shear components are expressed as

$$\boldsymbol{B}_I^b = \left[\begin{array}{ccc} 0 & \Psi_{I,1} & 0 \\ 0 & 0 & \Psi_{I,2} \\ 0 & \Psi_{I,2} & \Psi_{I,1} \end{array}\right], \quad \boldsymbol{B}_I^s = \left[\begin{array}{ccc} \Psi_{I,1} & -\Psi_I & 0 \\ \Psi_{I,2} & 0 & -\Psi_I \end{array}\right], \tag{13}$$

where $\Psi_{I,i}$ (i=1, 2) are the derivatives of the RKs with respect to the direction x_i.

To overcome the shear-locking effect in the meshfree method, Wang and Chen [15] analyzed KMRC for Mindlin-Reissner plate. When the nodal value $\boldsymbol{d}_I$ is represented as a pure bending deformation, the curvature, and shear strain in Eq.(12) can be satisfied as $\boldsymbol{\kappa}^h$=*const.* and $\boldsymbol{\gamma}^h$=0. To impose KMRC, the use of a complete quadratic basis is proposed with basis vector $\boldsymbol{H}(\boldsymbol{x})$, is given by

$$\boldsymbol{H}^T(\boldsymbol{x}) = \{1 \quad x_1 \quad x_2 \quad x_1^2 \quad x_1x_2 \quad x_2^2\}^T. \tag{14}$$

The shape of the RK $\Psi_I(\boldsymbol{x})$ is represented in Fig.2.

Additionally, an enriched basis is introduced to analyze shear deformable plate problems involving cracks. We examine two kinds of basis vectors

$$\boldsymbol{H}^T(\boldsymbol{x}) = \{1 \quad x_1 \quad x_2 \quad x_1^2 \quad x_1x_2 \quad x_2^2 \quad \sqrt{r}\}^T, \tag{15}$$

and

$$\boldsymbol{H}^T(\boldsymbol{x}) = \{1 \quad x_1 \quad x_2 \quad x_1^2 \quad x_1x_2 \quad x_2^2 \quad \sqrt{r}\sin(\delta/2)\}^T, \tag{16}$$

where r and δ are local polar coordinates from the crack tip. The enriched functions are introduced based on the enriched RK approximation in [41]. This is a convenient way to accurately capture the $1/\sqrt{r}$ stress-singularity of stresses around the crack tip in the meshfree approximation.

2.3. Numerical integration

SCNI [17] is introduced to accurately integrate the stiffness matrix for plate bending problems. The numerical integration technique satisfies the so-called integration constraint, which is a necessary condition for linear exactness in Galerkin-based meshfree methods. In addition, numerical instabilities arising from a spurious mode of the stiffness matrix employing direct nodal integration can be avoided. The strain components are smoothed by the Gauss divergence theorem. SCNI for plate bending problems are briefly reviewed.

A schematic for the mid-plane of the plate is given in Fig.3. The nodes are regularly distributed in the analysis model. A Voronoi cell diagram [42] is adopted to construct the model. The cells are automatically generated so as to surround each node. A cell belonging to the K-th node is depicted in Fig.3. The area is Ω_K, the boundary is Γ_K, and $\boldsymbol{n}$ is the normal of Ω_K. The curvature of Eq.(12) can be rewritten as

$$\tilde{\kappa}_{ij}(\boldsymbol{x}_K) = \frac{1}{A_K}\int_{\Omega_K} \kappa_{ij}(\boldsymbol{x}) d\Omega_K = \frac{1}{2A_K}\int_{\Omega_K} (\theta_{i,j} + \theta_{j,i}) d\Omega_K, \tag{17}$$

and for the shear strain

$$\tilde{\gamma}_i(\boldsymbol{x}_K) = \frac{1}{A_K}\int_{\Omega_K} \gamma_i(\boldsymbol{x}) d\Omega_K = \frac{1}{A_K}\int_{\Omega_K} (w_{,i} - \theta_i) d\Omega_K, \tag{18}$$

where $\tilde{\kappa}_{ij}(\boldsymbol{x}_K)$ and $\tilde{\gamma}_i(\boldsymbol{x}_K)$ are smoothed curvature and shear strain, respectively, defined in area Ω_K.

We employ the divergence theorem to Eqs.(17) and (18), which are thus represented as

$$\tilde{\kappa}_{ij}(\boldsymbol{x}_K) = \frac{1}{2A_K}\int_{\Gamma_K} (\theta_i n_j + \theta_j n_i) d\Gamma_K, \tag{19}$$

$$\tilde{\gamma}_i(\boldsymbol{x}_K) = \frac{1}{A_K}\left(\int_{\Gamma_K} w n_i d\Gamma - \int_{\Omega_K} \theta_i d\Omega_K\right), \tag{20}$$

where n_i $(i = 1, 2)$ denotes the x_i-component of the normal vector $\boldsymbol{n}$. A line integration along the boundary Γ_K is adopted Eq.(19) and the first term of the left hand side of Eq.(20). Additionally, a surface integal is adopted for the second term of the left hand side of Eq.(20). A five-point Gauss quadrature is adopted for the line integration Γ_K. A Voronoi cell is divided into triangles and a 13-point Gauss quadrature is adopted for each triangle in the surface integral Ω_K. In the SCNI, a physical value is evaluated on the nodes, and the uniform value is employed over the entire cell Ω_K. Further details of the discretization in Eq.(19) and (20) are presented in [15,18].

2.4. The principles of virtual work

A penalty formulation is applied to impose the essential boundary conditions. The principle of virtual work is written as

$$\int_{\Omega} (z^2 \delta\boldsymbol{\kappa}^T \boldsymbol{D}^b \boldsymbol{\kappa} + \delta\boldsymbol{\gamma}^T \boldsymbol{D}^s \boldsymbol{\gamma}) d\Omega + \alpha \int_{\Gamma^g} \delta\boldsymbol{d}(\boldsymbol{d} - \bar{\boldsymbol{d}}) d\Gamma - \delta W = 0, \tag{21}$$

where α is a penalty parameter. $\delta\boldsymbol{d}$ includes variation of the deflection and rotations. $\bar{\boldsymbol{d}}$ is an enforced value vector along the essential boundaries Γ^g. Substituting the displacement, curvature and shear strain of Eqs.(1), (19) and (20) into Eq.(21), and after rearranging the equation, we obtain the following

$$\left(\boldsymbol{K}_{IJ} + \boldsymbol{K}_{IJ}^p\right)\boldsymbol{d}_J = \left(\boldsymbol{f}_I + \boldsymbol{f}_I^p\right), \tag{22}$$

where $\boldsymbol{K}_{IJ}$ and $\boldsymbol{f}_I$ are, respectively, the global stiffness matrix and the force vector of the plate bending problem. $\boldsymbol{K}_{IJ}^p$ and $\boldsymbol{f}_I^p$ are the matrix and vector in terms of the penalty term. They are detailed as follows:

$$\boldsymbol{K}_{IJ} = \sum_{K=1}^{\mathrm{NP}} \boldsymbol{K}_{IJ}(\boldsymbol{x}_K), \tag{23}$$

$$\boldsymbol{f}_I = \sum_{K=1}^{\mathrm{Nb_{int}}} \boldsymbol{\Lambda}_I(\boldsymbol{x}_K) \left\{ \begin{array}{c} 0 \\ -\bar{M}_{11}(\boldsymbol{x}_K) \\ -\bar{M}_{22}(\boldsymbol{x}_K) \end{array} \right\} + \sum_{K=1}^{\mathrm{NP}} \boldsymbol{\Lambda}_I^T(\boldsymbol{x}_K) \left\{ \begin{array}{c} \bar{p}(\boldsymbol{x}_K) \\ 0 \\ 0 \end{array} \right\}. \tag{24}$$

$\mathrm{Nb_{int}}$ is the number of nodes along the prescribed moments. The stiffness matrix for K-th node is represented, as:

$$\boldsymbol{K}_{IJ}(\boldsymbol{x}_K) = \int_\Omega z^2 \boldsymbol{B}_I^{b^T}(\boldsymbol{x}_K)\boldsymbol{D}\boldsymbol{B}_J^b(\boldsymbol{x}_K)d\Omega + \int_\Omega \boldsymbol{B}_I^{s^T}(\boldsymbol{x}_K)\boldsymbol{D}\boldsymbol{B}_J^s(\boldsymbol{x}_K)d\Omega. \tag{25}$$

The three-point Newton-Cotes quadrature is adopted to integrate the plate thickness direction in Eq.(25). Additionally, the matrix and vector for the penalty term are presented as follows:

$$\boldsymbol{K}_{IJ}^p = \alpha \sum_{K=1}^{\mathrm{Ng_{int}}} \boldsymbol{\Lambda}_I^T(\boldsymbol{x}_K)\boldsymbol{\Lambda}_J(\boldsymbol{x}_K), \quad \boldsymbol{f}_I^p = \alpha \sum_{K=1}^{\mathrm{Ng_{int}}} \boldsymbol{\Lambda}_I^T(\boldsymbol{x}_K)\bar{\boldsymbol{d}}_I, \tag{26}$$

where $\mathrm{Ng_{int}}$ is the number of nodes along the essential boundary conditions. $\boldsymbol{\Lambda}_I$ in Eqs.(24) and (26) is a matrix of RKs used in imposing the external force and the essential boundary conditions.

$$\boldsymbol{\Lambda}_I = \begin{bmatrix} \Psi_I & 0 & 0 \\ 0 & \Psi_I & 0 \\ 0 & 0 & \Psi_I \end{bmatrix}. \tag{27}$$

3. Crack modeling and J-integral for the plate bending problems

3.1. Crack modeling

The visibility criterion and diffraction method [33-35] are adopted in crack modeling. SSCI [37] is employed to accurately integrate the stiffness matrix along the crack segment.

A rectangular plate containing an edge crack depicted in Fig.4(a), is considered. x'_1 and x'_2 are the local coordinates at the crack tip. (r,δ) are the local polar coordinates. Nodes are distributed over the mid-surface of the plate. A function support for the nodes is also presented. Voronoi cells are generated automatically to surround the nodes as shown in Fig.4(b). In crack modeling, the crack tip is placed on a node, and the crack segment is represented by assembly of the nodes. The details of crack modeling employing areas A and B in Fig.4(b) are now discussed.

In area A, the meshfree functions are across the crack segment. The visibility criterion and SSCI is adopted to cut the functions along the crack segment so as to represent the displacement discontinuity. The discontinuous meshfree function is presented in Fig.4(c). Originally, SSCI was introduced in plate bending problems by employing the Hermite RK approximation [37,38,43-45], and the numerical integration technique is used in crack modeling. A close-up view of area A is illustrated in Fig.4(d). When a crack segment cut a Voronoi cell, the cell is divided into a sum of triangles along the segment, and SCNI is applied to each triangle. The curvature and shear strain components are then rewritten as

$$\tilde{\kappa}_{ij}(\boldsymbol{x}_{K_i}) = \frac{1}{2A_{K_i}} \int_{\Gamma_{K_i}} (\theta_i n_j + \theta_j n_i) d\Gamma_{K_i}, \tag{28}$$

$$\tilde{\gamma}_i(\boldsymbol{x}_{K_i}) = \frac{1}{A_{K_i}} \left(\int_{\Gamma_{K_i}} w n_i d\Gamma - \int_{\Omega_{K_i}} \theta_i d\Omega_{K_i} \right), \tag{29}$$

where Γ_{K_i} is the boundary of the surface Ω_{K_i}, and n_i $(i = 1, 2)$ denote the x_1- and x_2-components of the normal vector to the boundary Γ_{K_i}. The physical values are evaluated for each center of gravity of the triangles. The strain and stress in the triangles Ω_{K_i} are smoothed.

In area B, a crack tip is located on a node. The diffraction method is adopted to represent the crack tip. The function support is corrected so as to wrap around the crack tip. The function shape at the crack tip is depicted in Fig.4(e). An illustration of the crack tip modeling employing the diffraction method is presented in Fig.4(f). When a line between a node and a quadrature point intersects a crack segment, and the crack tip is located within the support of the node, the meshfree shape functions are modified using the s-dependent spline function given in Eq.(10); s is determined by

$$s = \left(\frac{s_1 + s_2(\boldsymbol{x})}{s_0(\boldsymbol{x})} \right)^{\lambda} \frac{s_0(\boldsymbol{x})}{h}, \tag{30}$$

where $s_0(\boldsymbol{x}) = ||\boldsymbol{x} - \boldsymbol{x}_I||$, $s_1 = ||\boldsymbol{x}_{TIP} - \boldsymbol{x}_I||$ and $s_2(\boldsymbol{x}) = ||\boldsymbol{x} - \boldsymbol{x}_{TIP}||$. λ is a shape factor set to λ=1. SSCI is adopted for the cell at the crack tip. The modifications of the meshfree interpolants are employed for the approximation functions of the deflection and rotation components in Eq.(11).

3.2. SIFs in the Mindlin-Reissner plate

A through-thickness crack is considered in a shear deformable plate as shown in Fig.1. There are three kinds of moment and shear force intensity factors in the plate fracture mechanics. The deformation modes are presented in Figs.5(a)-(c) which corresponds to symmetric bending, anti-symmetric bending, and shear modes. The quantities are corresponds to K_1, K_2 and K_3. They are defined as: $K_1 = \lim_{r \to 0} \sqrt{2r}\, M_{22}(r,0)$, $K_2 = \lim_{r \to 0} \sqrt{2r}\, M_{12}(r,0)$, and $K_3 = \lim_{r \to 0} \sqrt{2r}\, Q_2(r,0)$, respectively. M_{22} and M_{12} are moments, and Q_2 is the shear force applied to the cracked plate. In this research, the moment intensity factor K_1 is only treated in the numerical examples.

3.3. A path-independent integral

3.3.1. J-integral for the plate bending problem

A path-independent integral is adopted to evaluate the moment intensity factor in a cracked plate. An illustration of the edge crack problem and the J-integral evaluation is presented in Fig.6(a). The J-integral for the shear deformable plate was proposed in [39,40],

$$J_k = \int_{\Gamma_{Jint}} \left(W\delta_{k\beta} - [M_{\alpha\beta}\theta_{\alpha,k} + Q_\beta w_{,k}] \right) n_\beta d\Gamma_{Jint}, \quad (k = 1, 2) \tag{31}$$

where the open contour Γ_{Jint} surrounds the crack tip. ds is a segment of Γ_{Jint}, and n_β is normal to the Γ_{Jint}. A comma indicates partial differentiation. The strain energy in shear deformation W is

$$W = \frac{1}{2}[M_{\alpha\beta}\theta_{\alpha,\beta} + Q_\beta\,(\theta_\beta + w_{,\beta})], \tag{32}$$

where α and β are indices corresponding to the x_1- and x_2-directions. The J_1-integral is path-independent, and its magnitude is equivalent to the energy release rate corresponding to a unit crack advance in the x_1'-direction.

3.3.2. J-integral discretization employing the nodal integration

The discretization of the J-integral in the meshfree method is presented. Because SCNI and SSCI are employed in the numerical integration of the stiffness matrix, the nodal integration is also used in the J-integral evaluation. The meshfree discretization with the Voronoi cells for the edge crack problem is shown in Fig.6(b). The segment ds is determined by the distance between nodes in surrounding the crack tip. The path includes some of the Voronoi cells that are integration domains for SCNI and SSCI. The J-integral of Eq.(31) is discretized by SCNI and SSCI, as:

$$\begin{aligned}\tilde{J}_k = &\sum_{i=1}^{N_{SCNI}} \left(\tilde{W}\delta_{k\beta} - \left[\tilde{M}_{\alpha\beta}\tilde{\theta}_{\alpha,k} + \tilde{Q}_\beta\tilde{w}_{,k}\right]\right) n_\beta ds_i \\ &+ \sum_{j=1}^{N_{SSCI}} \left(\tilde{W}\delta_{k\beta} - \left[\tilde{M}_{\alpha\beta}\tilde{\theta}_{\alpha,k} + \tilde{Q}_\beta\tilde{w}_{,k}\right]\right) n_\beta ds_j, \quad (k = 1, 2)\end{aligned} \tag{33}$$

where ($\tilde{}$) in Eq.(33) signifies smoothed physical values evaluated by the nodal integration, and N_{SCNI} and N_{SSCI} denote the number of segments used for the nodal integration. ds_i and ds_j are the lengths of the segments. Typical segments for SCNI and SSCI are indicated in Figs.7(a) and (b), respectively. Two segments ds_i are needed for each Voronoi cell in SCNI. The physical quantities defined by each node are employed as the two segments for evaluating the J-integral. Additionally, a segment ds_j is employed for each triangle in SSCI. The smoothed physical values defined at the center of gravity are employed.

The J-integral evaluation using nodal integration is effective not only because smoothed values are used but also because computational efficiency is enhanced. Because the J-integral is evaluated by the sum of the physical quantities in post processing, Gauss quadrature rule is therefore not required.

4. Numerical examples and discussions

Several numerical examples for shear deformable plates involving cracks are analyzed to examine the proposed technique. The function support of the RK is set to h=1.2h^p, where h^p is the characteristic spacing between nodes in the meshfree models. Young's modulus E=210 (GPa), Poisson's ratio ν=0.3, and penalty coefficient α=1e+7 are used in all the numerical examples unless stated otherwise.

4.1. A rectangular plate involving a centered crack

A centered crack on a plate is analyzed. The analysis model is presented in Fig.8(a). The width and length of the plate are 2b and 2c, respectively. The crack size is 2a, and the plate thickness is t. As the boundary conditions, the two edges parallel to the crack are simply supported, and moment M is applied to the edges; the other two edges are free. In addition to the visibility criterion and diffraction method, three basis vectors $\boldsymbol{H}(\boldsymbol{x})$ in Eqs.(14), (15), and (16) are employed in the crack modeling. They are referred to as the no enrichment, enriched bases A and B. When a crack tip is located within a support of the RKs, the enriched terms $\sqrt{r}$ and $\sqrt{r}\sin(\delta/2)$ are introduced into the RKs using the enriched bases A and B, respectively.

The accuracy of the moment intensity factor K_1 and the path independency of the J-integral are examined first. The size of the cracked plate is 2b=1,000 (mm), 2c=2,000 (mm), and t=250 (mm). The crack length is 2a=400 (mm). In meshfree plate modeling, the nodes are regularly and irregularly distributed on the plate. Three kinds of divisions are employed for the regular and irregular models. They have 21×41, 41×81, and 81×161 nodes. Close-up views of the regular and irregular models (41×81 nodes) around the crack are presented in Figs.8(b) and (c). Additionally, the different paths for the J-integral are chosen by a region $2l_d \times 2l_d$ centered around the crack tip, as shown in Figs.8(b) and (c). The no enrichment is chosen. For numerical integration of the stiffness matrix and the J-integral, SCNI is adopted over the entire model and SSCI is only adopted along the crack segment.

The numerical results are presented in Figs.9(a) and (b) for regular and irregular models. The moment intensity factor is normalized by $F_1{=}K_1/M\sqrt{\pi a}$. The reference solution is F_1^{Ref}=0.8694 in [46]. Although the accuracy improves as the density of the nodes increases, the normalized moment intensity factors F_1 oscillate. The path dependency can be found in both the regular and irregular models.

To further examine the accuracy of the solution and the path independency of the J-integral, SSCI is employed over the entire analysis domain. The no enrichment is also employed. The numerical results are presented in Figs.10(a) and (b) for the regular and irregular models. Although the accuracy is almost the same as the results presented in Figs.9(a) and (b), path independency can be achieved in both models. It is found that the use of SSCI enhances path independency of the J-integral. Although F_1 approaches the reference solution as the density of nodes increases, there are some discrepancies even for a fine set of 81×161 scattered nodes.

The convergence of F_1 for no enrichment, enriched bases A and B is analyzed. The four regular models (11×21, 21×41, 41×81 and 81×161 nodes) are adopted, and the percentage error in F_1 is examined. The error is defined, as: Error=$|F_1$-$F_1^{Ref}|/F_1^{Ref}\times 100$ (%). The size of the path for the J-integral is set to l_d=200 (mm) for all the models. SSCI is employed over the entire analysis domain. The results are presented in Fig.11. h^p is the node spacing in the meshfree models. All results with the no enrichment, enriched basis A, and B uniformly converge as nodal density increases. When employing basis B, the accuracy is significantly improved compared with the results with no enrichment and bases A. In addition, the difference of the F_1 between 41×81 nodes model and the reference solution is less than 0.1% when employing the enriched basis B. Almost same accuracy is obtained when employing 81×161 nodes model. Because the reference solution is not an exact solution, it is thus considered that the results 41×81 and 81×161 nodes models are converged.

In addition, path independency of the enriched basis B with different paths is assessed in Fig.12(a) and (b) for the regular and irregular models. In both cases, the present results are in good agreement with the reference solution, and path independency is fulfilled in all the meshfree models. Clearly, highly accurate results are obtained when employing 41×81 nodes models for the crack length $2a$=400 (mm). For a single crack problem, we derive a relation $a/h^p > 8.0$ between the crack length and the node spacing h^p to evaluate the J-integral with high accuracy. We then employ the basis B and the criterion in the following numerical examples with single crack.

To further examine the accuracy of the enrichment techniques, the stress distributions $\boldsymbol{\sigma}_{22}$ near the crack tip are examined. The results are presented in Fig.13. The regular model (41×81 nodes) is applied, and the three enrichment techniques are compared. As a reference solution, MSC.MARC is adopted. Very fine FE model is employed, and thick-plate shell element (element number 75 in MSC.MARC) is chosen. In the FE analysis, the degrees of freedom for the deformations of the x_1- and x_2-directions are fixed because the membrane deformation is not considered. It can be observed that the enriched basis B is good agreement with the reference solution. It is confirmed that high accuracy stress distributions are obtained than the other enrichment techniques.

Furthermore, eigenvalues analysis is carried out for the stiffness matrix $\boldsymbol{K}_{IJ}$ in Eq.(25). The condition number is defined as $\kappa(\boldsymbol{K}_{IJ}) = |\lambda_{\max}/\lambda_{\min}|$. $\lambda_{\max}$ and $\lambda_{\min}$ are the maximum and minimum eigenvalues. The results are $\kappa(\boldsymbol{K}_{IJ})$=2.30e+8, 2.34e+8 and 2.31e+8, for no enrichment, enriched basis A and B, respectively. There are few differences in the condition number.

The effectiveness is confirmed in using SSCI for the J-integral evaluation in the meshfree method. However, extra effort is required to assemble the stiffness matrix when SSCI is used over the entire analysis domain. Hence, SSCI is only adopted around the crack. An illustration of the meshfree modeling is given in Fig.14(a) and (b) for the regular and irregular models. With the center crack length set to $2a$, SSCI is employed for the Voronoi cells associated with the nodes within an area of width $4a$ and height $2a$ centered on the crack. The J-integral is evaluated within the area of SSCI as shown in Fig.14(a) and (b).

K_1 is evaluated employing the proposed technique with a/t=0.8 (200/250), 1.0 (250/250), 4.0 (200/50) and 5.0 (250/50) for both regular and irregular models. The computed numerical results for a/t are presented in Table 1 along with reference solutions for comparison [25,46]. Good agreement has been obtained. It is apparent that the normalized moment intensity factor decreases with increasing ratio a/t.

4.2. Rectangular plate with symmetric edge cracks

Symmetric edge cracks in a rectangular plate, as shown in Fig.15(a) are analyzed. The plate width and length are $2b$=1000 (mm) and $2c$=2000 (mm). The plate thickness is t=50 and 250 (mm). Meshfree models (41×81 nodes) are presented in Figs.15(b) and (c) for regular and irregular models. The crack length a=300 (mm) and the distance between the cracks $2d$=400 (mm). The boundary conditions are the same as the center crack problem in Section 4.1. The plate width $2b$ is fixed, and F_1 is evaluated for various t and d. To accurately represent the severe stress concentration between the crack tips, an relation $d/h^p > 6.0$ in addition to $a/h^p > 8.0$.

The numerical results calculated using the proposed method are presented in Tables 2 and 3 for b/t=2.0 and 10.0. The ratio d/b is varied from 0.2 to 0.6. As expected, the results obtained using the developed meshless method for all d/b values show good correlation with the reference solutions [46]. More interestingly, deviations of the numerical results obtained with the irregular model are insignificant, implying that the proposed meshfree method performs well for both regular and irregular discretized nodes. This consequence definitely is an additional advantage of the present formulation as most of the problem domains in practice are usually more complicated and irregular models are often used instead. From the tables, it is very interesting to observe that the normalized moment intensity factor decreases with increasing d/b. This indicates a clear finite-size effect in the model.

4.3. Edge crack in a rectangle plate

A rectangular plate with an edge crack is analyzed. The analysis model is presented in Fig.16 (a), The model size is b=1000 (mm) and c=2000 (mm). The plate thickness is 100 and 500 (mm). Meshfree models (41×81 nodes) for crack length a=500 (mm) are presented in Fig.16(b) and (c) for both regular and irregular models.

The factor F_1 is evaluated for different crack lengths a varying both the plate thickness t and plate width b. The problems were solved in [25]. The graph in [25] was digitized and results compared. The numerical results for b/t=2.0 and 10.0 are presented in Figs.17(a) and (b) for regular and irregular models. The results coincide with the reference solution in all cases. From

Fig.17 that, the ratio is found to b/t greatly alters the normalized moment intensity factor.

4.4. Single crack emanating from a hole

The last numerical example deals with a finite-width rectangle plate with a single crack emanating from a hole. The analysis model is presented in Fig.18(a). The plate width b=1000 (mm) and c=2000 (mm). The plate thickness t=125 and 250 (mm), and the hole radius r_h=50 and 125 (mm) are adopted. The hole radius is r_h and the crack length is $a - r_h$. The meshfree models (41 × 81 nodes) are presented in Figs.18(b) and (c), for regular and irregular models. The radius r_h=125 (mm) and a is 400 (mm). The meshfree model is automatically generated by employing a Voronoi cell diagram [42].

F_1 is evaluated by varying a and t. The problems were solved in [25] and the data was extracted for comparison purpose. The results are presented in Figs.19(a) and (b) for regular and irregular models, and shows that the present results calculated by the developed meshfree method match well the reference solutions for all aspect ratios r_h/b and b/t. Once again, the numerical results reveal no effect on the normalized moment intensity factor when using the irregular models.

5. Conclusion

Cracked plate problems were numerically analyzed using a novel enriched meshfree approach based on the Mindlin-Reissner plate formulation. A visibility criterion, diffraction method, and enriched basis are introduced to model a crack in the shear deformable plate. SCNI and SSCI are employed to accurately represent the cracked plate in the meshfree method. A novel technique to evaluate the moment stress intensity factor employing SCNI and SSCI was proposed. The accuracy of the normalized moment intensity factors and the path independence of the J-integral are illustrated in a series of numerical examples. The developed meshfree method is found to offer solutions with high accuracy for the intensity factors of the cracked bending plates. The path independence is confirmed. The effect of irregular discretization on the normalized moment intensity factor is very small. All the results derived from irregular nodes are in good agreement with both the regular models and reference solutions. Several aspect ratios were numerically investigated and discussed. The developed meshfree method has potential, generality, and no limitations in extending to other engineering problems.

Acknowledgements

This research was partially supported by JSPS KAKENHI Grant-in-Aid for Scientific Research (A)(15H02328), (B)(15H04212) and (C)(15K06632). This work was performed under the Cooperative Research Program of the Joining and Welding Research Institute, Osaka University. Tinh Quoc Bui gratefully acknowledges the support from the Grant-in-Aid for Scientific Research (No. 26-04055) - JSPS.

References

[1] He W, Liu J, Xie D. Numerical study on fatigue crack growth at at web-stiffener of ship structural details by an objected-oriented approach in conjunction with ABAQUS. Mar Struct 2014;35:45-69.

[2] Qiao W, Sun J, Xie D. Development of super element to perform direct analysis on failure assessment of hull structures based on FAD. Mar Struct 2014;39:373-94.

[3] Tanaka S, Kawahara T, Okada H. Study on crack propagation simulation of surface crack in welded joint structure. Mar Struct 2014;39:315-34.

[4] Gotoh K, Niwa T, Anai Y. Numerical simulation of fatigue crack propagation under tensile loadings with phase differences. Mar Struct 2015;42:53-70.

[5] Anderson TL. Fracture Mechanics: Fundamentals and Applications Third Edition. Taylor & Francis; 2005.

[6] Sih GC (ed.). Plates and shells with cracks. Mechanics of Fracture Vol.3; 1997.

[7] Zhender AT, Viz MJ. Fracture mechanics of thin plates and shells under combined membrane, bending and twisting loads. Appl Mech Rev 2005;58:37-48.

[8] Belytschko T, Lu YY, Gu L. Element-free Galerkin Methods. Int J Numer Meth Eng 1994;37:229-56.

[9] Liu WK, Jun S, Zhang YF. Reproducing kernel particle methods. Int J Numer Meth Fluid 1995;20:1081-106.

[10] Wang D, Chen P. Quasi-convex reproducing kernel meshfree method. Comput Mech 2014;54:689-709.

[11] Atluri SN, T. Zhu. A new meshless local Petrov-Galerkin (MLPG) approach in computational mechanics. Comput Mech 1998;22:117-27.

[12] Bui QT, Nguyen NM, Zhang Ch. A meshfree model without shear-locking for free vibration analysis of first-order shear deformable plates. Eng Struct 2011;33:3364-3380.

[13] Bui QT, Nguyen NM, Zhang Ch. Buckling analysis of Reissner-Mindlin plates subjected to in-plane edge loads using a shear-locking-free and meshfree. Eng Anal Bound Elem 2011;35:1038-1053.

[14] Nguyen VP, Rabczuk T, Bordas S, Duflot M. Meshless methods: A review and computer implementation aspects. Math Comput Simulat 2008;79:763-813.

[15] Wang D, Chen JS. Locking-free stabilized conforming nodal integration for meshfree Mindlin-Reissner plate formulation. Comput Meth Appl Mech Eng 2004;193:1065-83.

[16] Wang D, Sun Y. A Galerkin meshfree method with stabilized conforming nodal integration for geometrically nonlinear analysis of shear deformable plates. Int J Comput Meth 2011;8:685-703.

[17] Chen JS, Wu CT, Yoon S, You Y. A stabilized conforming nodal integration for Galerkin meshfree methods. Int J Numer Meth Eng 2001;50:435-66.

[18] Sadamoto S, Tanaka S, Okazawa S. Elastic large deflection analysis of plates subjected to uniaxial thrust using meshfree Mindlin-Reissner formulation. Comput Mech 2013;52:1313-30.

[19] Moës N, Dolbow J, Belytschiko T. A finite element method for crack growth without remeshing. Int J Numer Meth Eng 1999;46:131-50.

[20] Dolbow J, Moës N, Belytschko T. Modeling fracture in Mindlin-Reissner plates with the extended finite element method. Int J Solid Struct 2000;37:7161-83.

[21] Liu P, Bui QT, Zhu D, Yu TT, Wang JW, Yin SH, Hirose S. Buckling failure analysis of cracked functionally graded plates by a stabilized discrete shear gap extended 3-node triangular plate element. Compos B Eng 2015;77:179-193.

[22] Yu TT, Bui QT, Liu P, Hirose S. A stabilized discrete shear gap extended finite element for the analysis of cracked Reissner-Mindlin plate vibration problems involving distorted meshes. Int J Mech Mater Des 2015;10.1007:s10999-014-9282-x.

[23] Lasry J, Pommier J, Renard Y, Salaün M. eXtended finite element methods for thin cracked plates with Kirchhoff-Love theory. Int J Numer Meth Eng 2010;84:1115-38.

[24] Dirgantara T, Aliabadi MH. Dual boundary element formulation for fracture mechanics analysis of shear deformable shells. Int J Solid Struct 2001;38:7769-800.

[25] Dirgantara T, Aliabadi MH. Stress intensity factors for cracks in thin plates. Eng Fract Mech 2002;69:1465-86.

[26] Aliabadi MH. A new generation of boundary element methods in fracture mechanics. Int J Fract 1997;86:91-125.

[27] Areias PMA, Song JH, Belytschko T. Analysis of fracture in thin shells by overlapping paired elements. Comput Meth Appl Mech Eng 2006;195:5343-60.

[28] Rabczuk T, Areias PMA, T. Belytschko. A meshfree thin shell method for non-linear dynamic fracture. Int J Numer Meth Eng 2007;72:524-48.

[29] Rabczuk T, Zi G, Gerstenberger A, Wall WA. A new crack tip element for the phantom-node method with arbitrary cohesive cracks. Int J Numer Meth Eng 2008;75:577-99.

[30] Chau-Dinh T, Zi G, Lee P-S, Rabczuk T, Song J-H. Phantom-node method for shell models with arbitrary cracks. Comput Struct 2012;92-93:242-56.

[31] Grandeep Bhardwaj, Singh IV, Mishra BK, Bui QT. Numerical simulation of functionally graded cracked plates using NURBS based XIGA under different loads and boundary conditions. Compos Struct 2015;126:347-359.

[32] De Luycker E, Benson DJ, Belytschko T, Bazilevs Y, Hsu MC. X-FEM in isogeometric analysis for linear fracture mechanics. Int J Numer Meth Eng 2011;87:541-65.

[33] Organ D, Fleming M, Terry T, Belytschko T. Continuous meshless approximations for nonconvex bodies by diffraction and transparency. Comput Mech 1996;18:225-35.

[34] Krysl P, Belytschko T. Element-free Galerkin method: Convergence of the continuous and discontinuous shape functions. Comput Meth Appl Mech Eng 1997;148:257-77.

[35] Fleming M, Chu YA, Moran B, Belytschko T. Enriched element-free galerkin methods for crack tip fields. Int J Numer Meth Eng 1997;40:1483-504.

[36] Mohammad M, Hossein MS, Reza N. RKPM approach to elastic-plastic fracture mechanics with notes on particles distribution and discontinuity criteria. Comput Model Eng Sci 2011;76:19-60.

[37] Wang D, Chen JS. A Hermite reproducing kernel approximation for thin-plate analysis with sub-domain stabilized conforming integration. Int J Numer Meth Eng 2008;74:368-90.

[38] Wang D, Peng H. A Hermite reproducing kernel Galerkin meshfree approach for buckling analysis of thin plates. Comput Mech 2013;51:1013-1029.

[39] Sosa HA, Eischen JW. Computation of stress intensity factors for plate bending via a path-independent integral. Eng Fract Mech 1986;25:451-62.

[40] Sosa H, Herrmann G. On invariant integrals in the analysis of cracked plates. Int J Fract 1989;40:111-26.

[41] Joyot P, Trunzler J, Chinesta F. Enriched reproducing kernel approximation: Reproducing functions with discontinuous derivatives. Lecture Notes in Computational Science and Engineering 2005;43:93-107.

[42] http://www.qhull.org/ [accessed 20.4.15]

[43] Wang D, Lin Z. Free vibration analysis of thin plates using Hermite reproducing kernel Galerkin meshfree method with sub-domain stabilized conforming integration. Comput Mech 2010;46:703-19.

[44] Wang D, Lin Z. Dispersion and transient analyses of Hermite reproducing kernel Galerkin meshfree method with sub-domain stabilized conforming integration for thin beam and plate structures. Comput Mech 2011;48:47-63.

[45] Tanaka S, Sadamoto S, Okazawa S. Nonlinear thin-plate bending analyses using the Hermite reproducing kernel approximation. Int J Comput Meth 2012;9:1240012.

[46] Boduroglu H, Erdogan F. Internal and edge cracks in a plate of finite width under bending. J Appl Mech Trans ASME 1983;50:621-7.

[47] Joseph PF, Erdogan F. Bending of a thin Reissner plate with a through crack. J Appl Mech Trans ASME 1991;53:842-6.

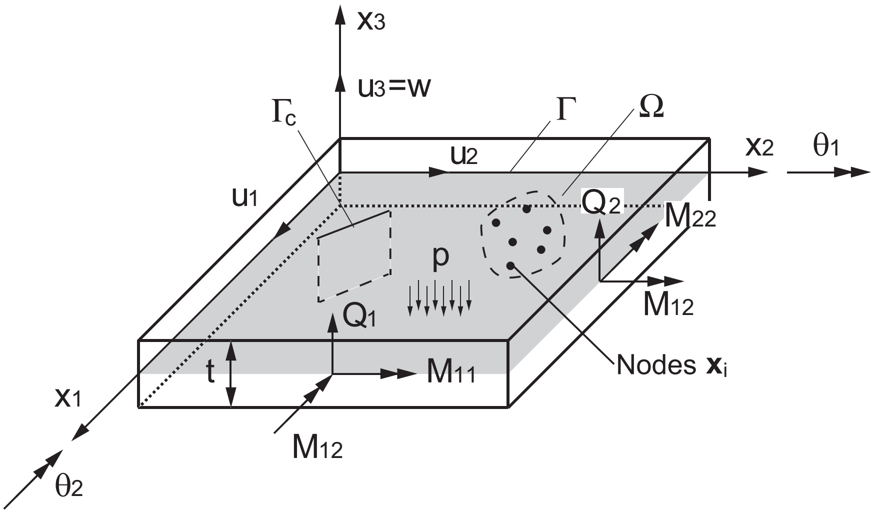

Figure 1: Schematic of a Mindlin-Reissner shear deformable plate.

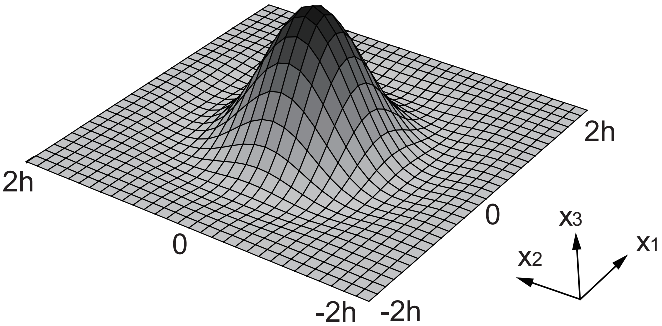

Figure 2: Schematic of a typical RK shape function in 2D.

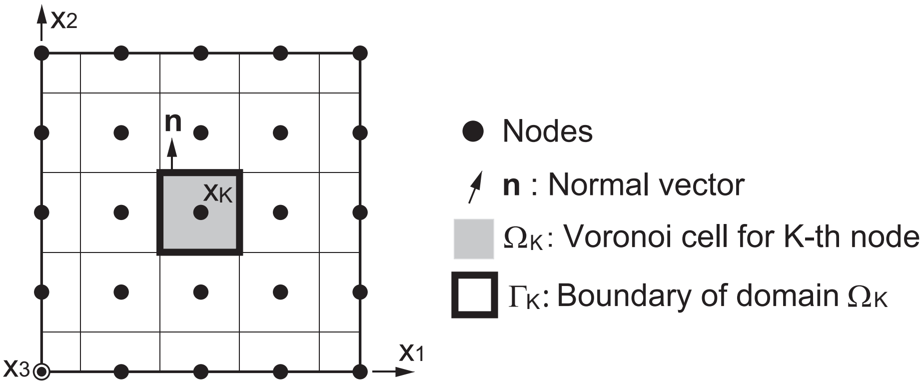

Figure 3: Schematic of mid-plane of the plate and the meshfree discretization with SCNI.

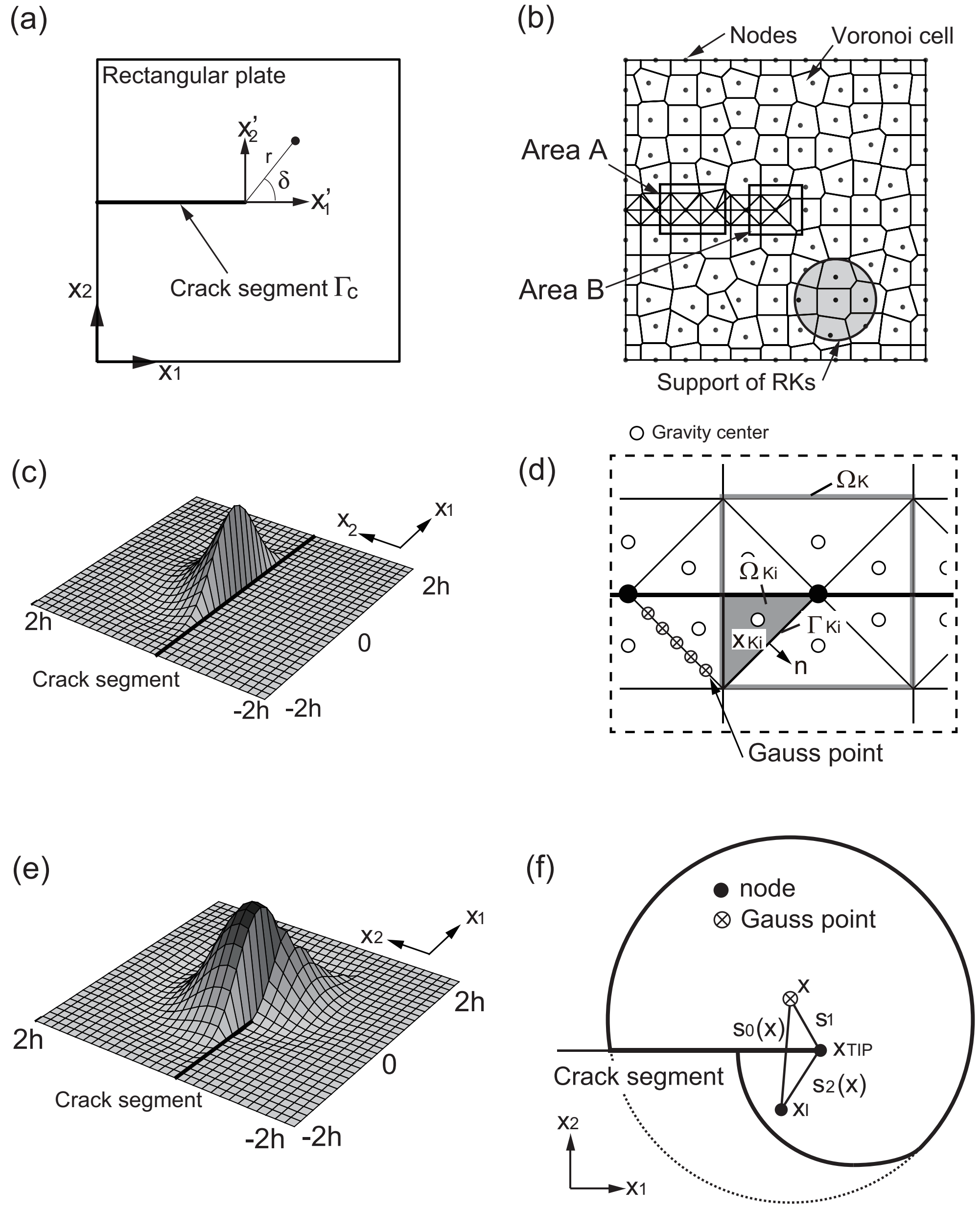

Figure 4: Crack modeling. (a) Single edge crack in a rectangular plate; (b) Meshfree model using Voronoi cell; (c) A modified meshfree function along the crack segment; (d) Modeling of crack segment with SSCI; (e) A modified meshfree function at the crack tip; (f) Modification of the meshfree function using the diffraction method.

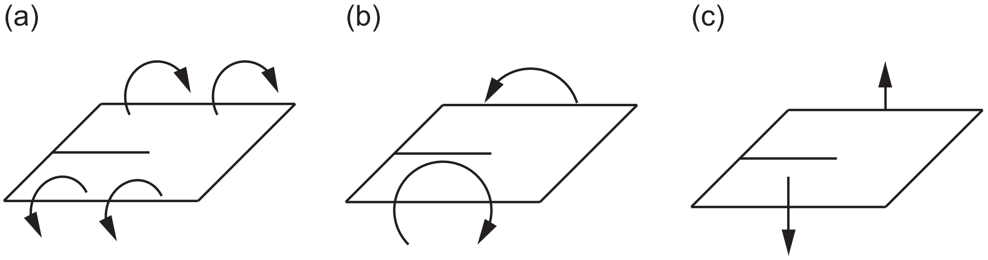

Figure 5: A moment and shear force intensity factors for a cracked shear deformable plate. (a) Symmetric bending mode K_1; (b) Anti-symmetric bending mode K_2; (c) Shear mode K_3.

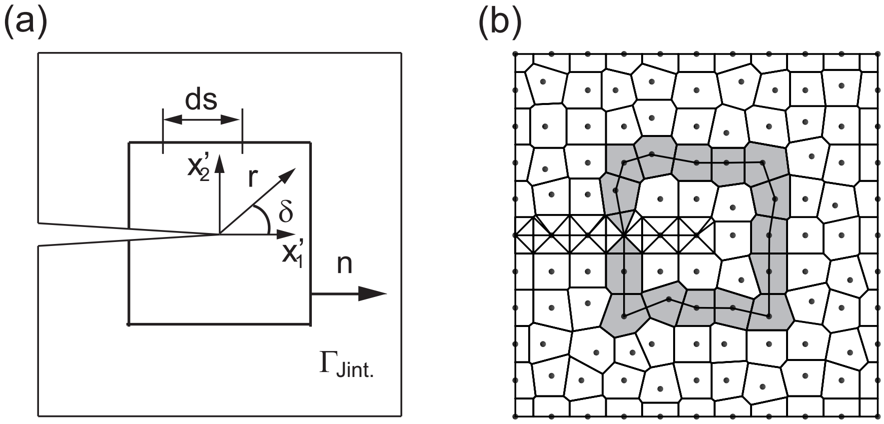

Figure 6: J-integral. (a) J-integral for an edge crack problem; (b) A discretization of the J-integral in the meshfree method.

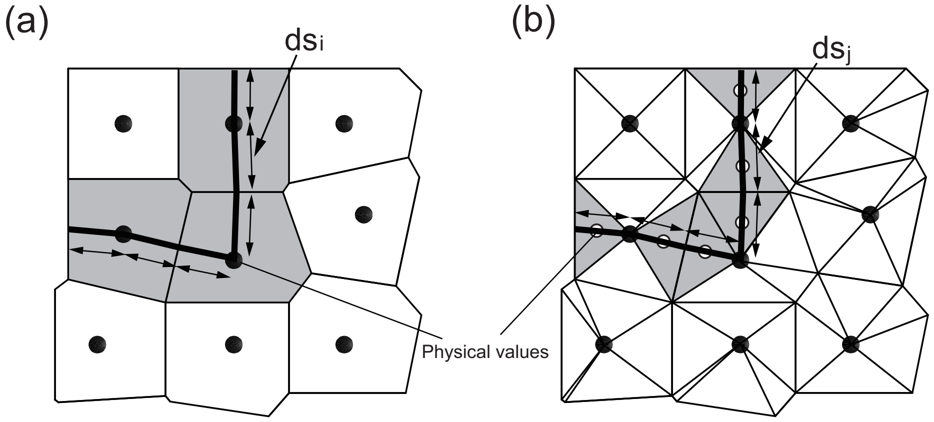

Figure 7: The segments for the J-integral evaluated by the nodal integration. (a) SCNI; (b) SSCI.

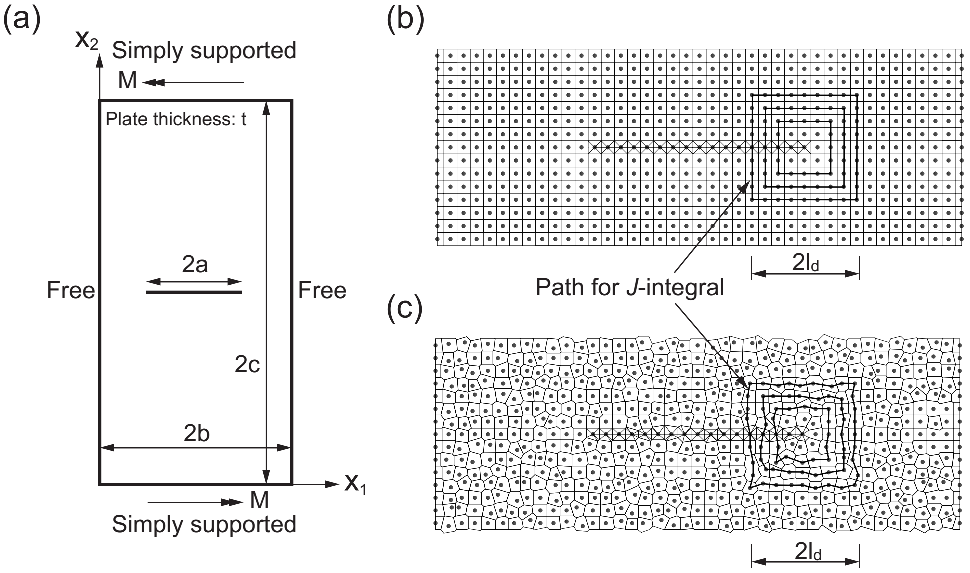

Figure 8: Centered crack in a rectangular plate. (a) Analysis model; (b) Regular model (41×81 nodes); (c) Irregular model (41×81 nodes).

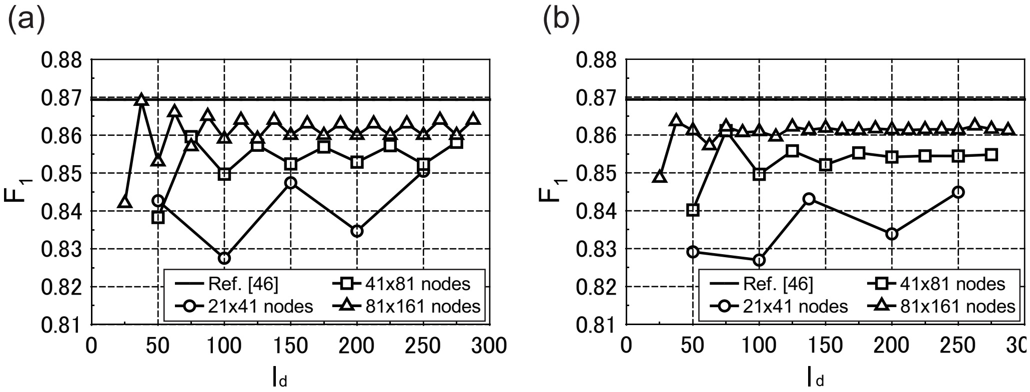

Figure 9: Normalized moment intensity factor for the different path with SCNI and SSCI (No enrichment). (a) Regular model; (b) Irregular model.

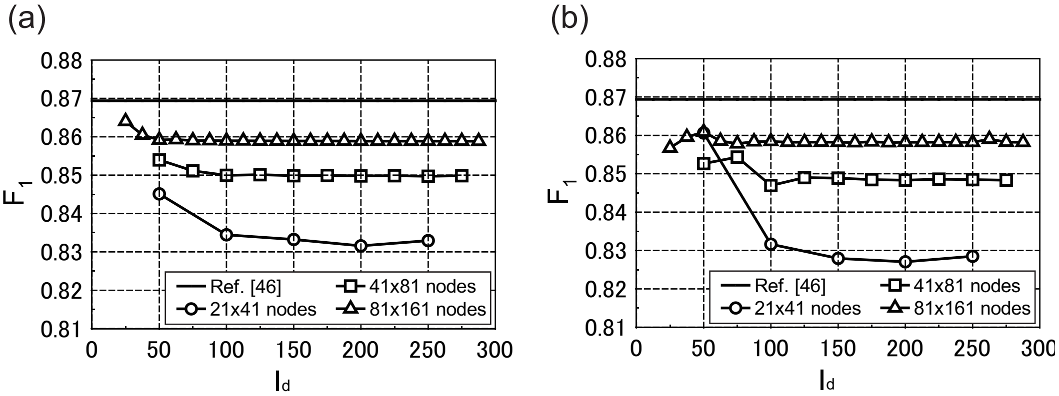

Figure 10: Normalized moment intensity factors for different paths with SSCI (No enrichment). (a) Regular model; (b) Irregular model.

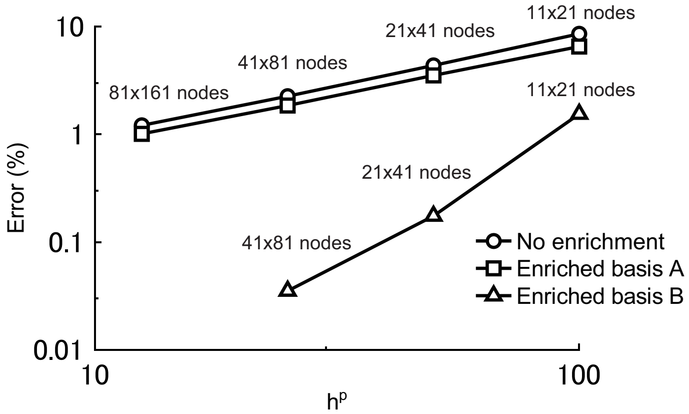

Figure 11: Convergence study employing no enrichment, enriched bases A, and B with SSCI.

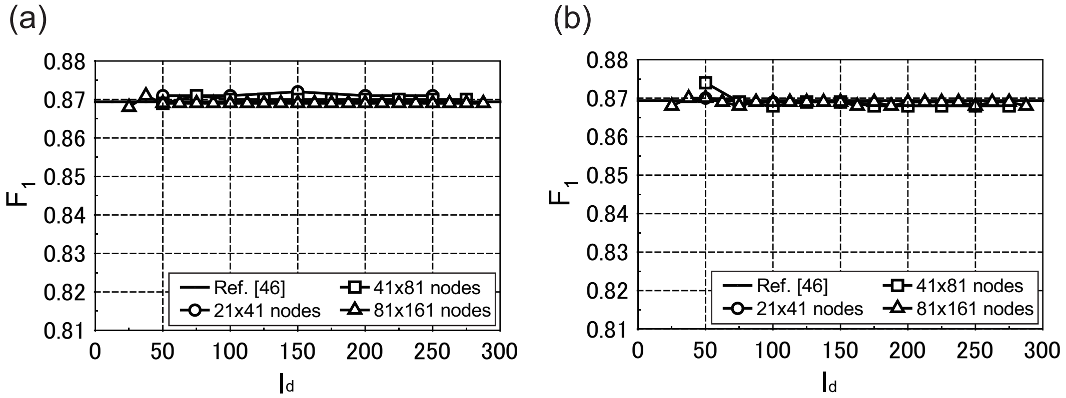

Figure 12: Normalized moment intensity factors for different path with SSCI (Enriched basis B). (a) Regular model; (b) Irregular model.

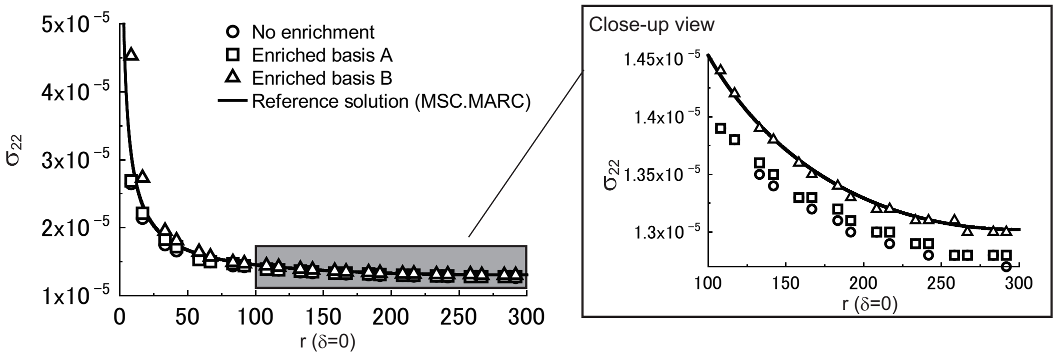

Figure 13: Stress distributions near the crack tip.

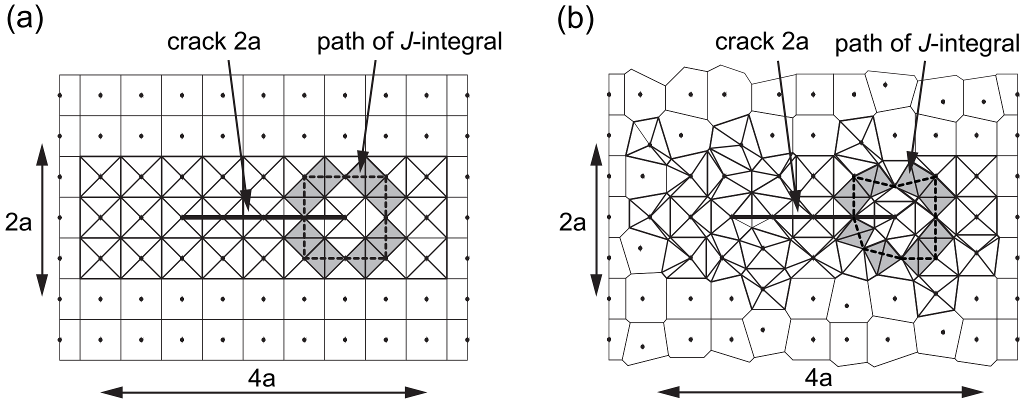

Figure 14: A meshfree modeling with SCNI and SSCI. (a) Regular model; (b) Irregular model.

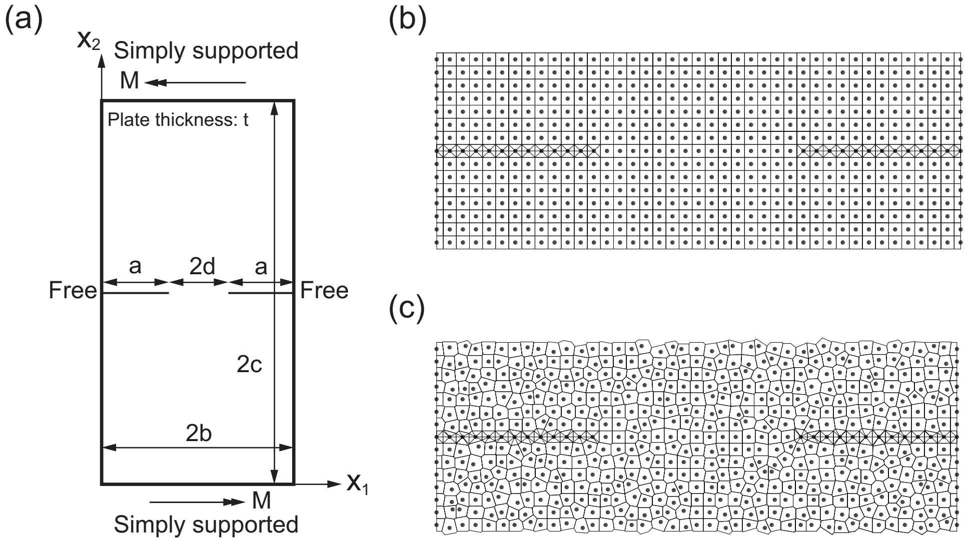

Figure 15: Symmetric edge cracks in a square plate. (a) Analysis model; (b) Regular model (41×41 nodes); (c) Irregular model (41×41 nodes).

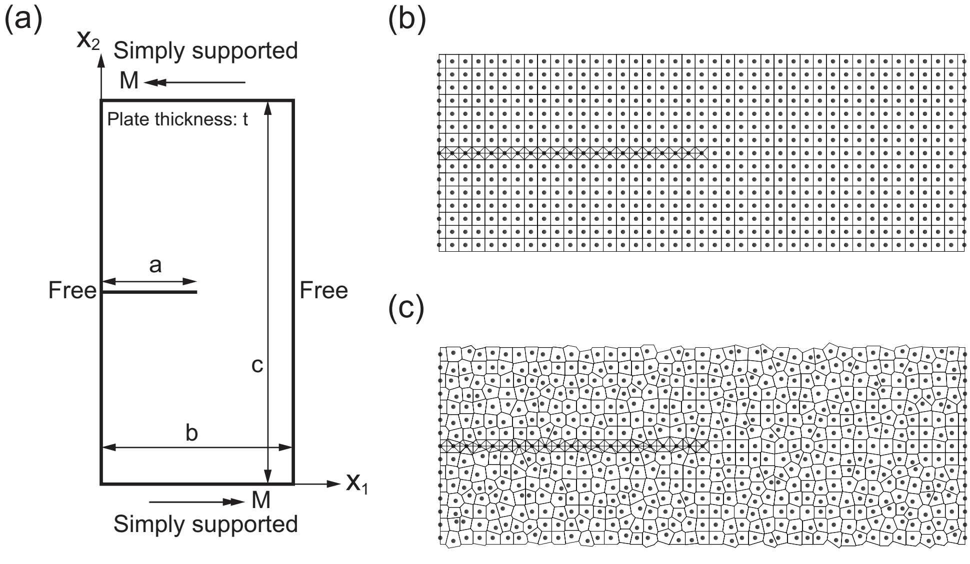

Figure 16: Single edge crack in a rectangle plate. (a) Analysis model; (b) Regular model (41×81 nodes); (c) Irregular model (41×81 nodes).

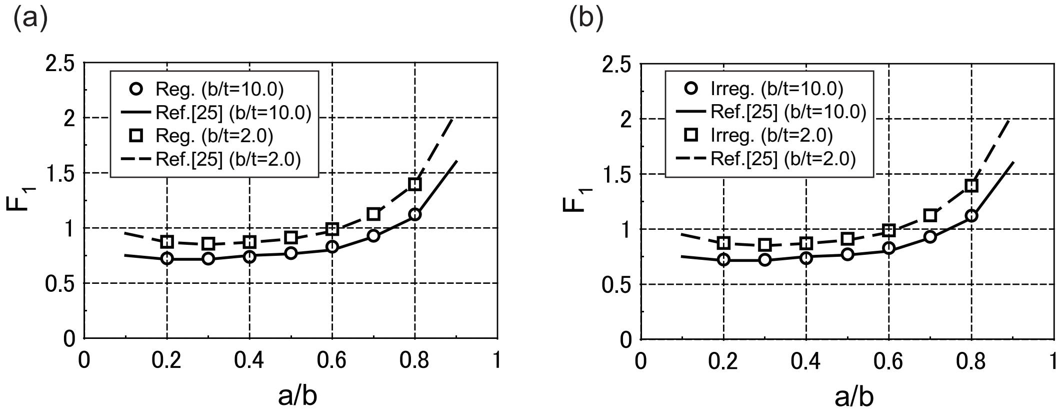

Figure 17: Normalized moment intensity factors for two plate thickness and varying crack length.

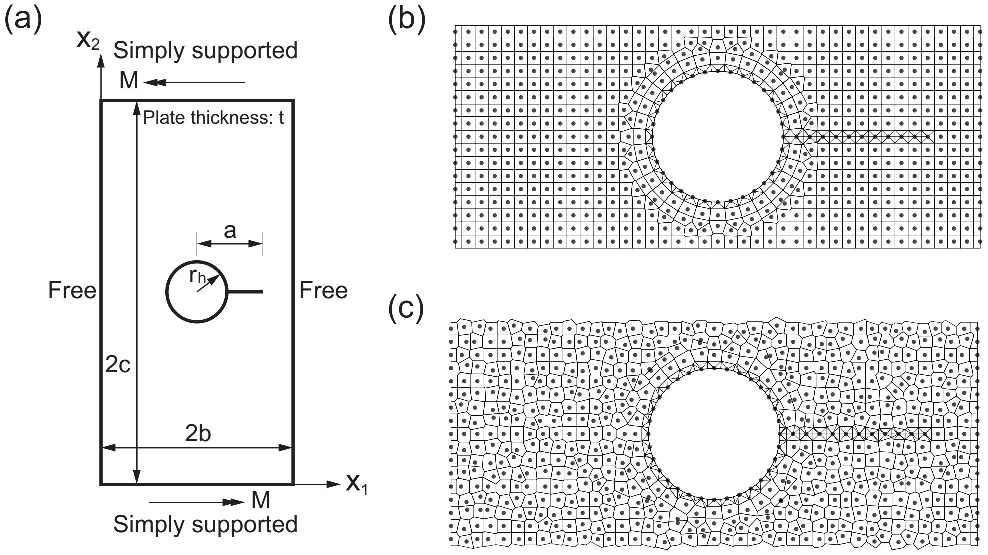

Figure 18: Finite width rectangle plate with a single crack emanating from a hole. (a) Analysis model; (b) Regular model (41 × 81 nodes); (c) Irregular model (41 × 81 nodes).

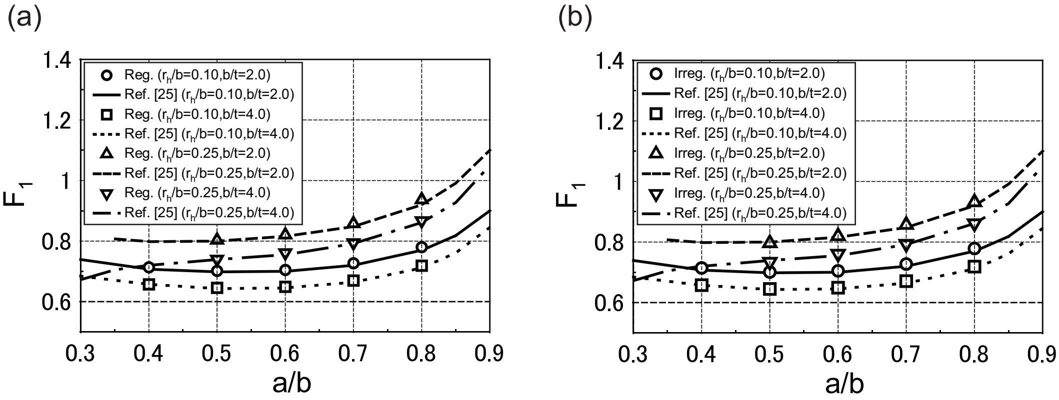

Figure 19: Normalized moment intensity factor. (a) Regular model; (b) Irregular model.

Table 1: Normalized moment intensity factor F_1 (Center crack problem).

a/t	0.8	1.0	4.0	5.0
Regular model	0.8699	0.9107	0.7312	0.7677
Irregular model	0.8683	0.9096	0.7287	0.7663
Ref.[46]	0.8694	0.9094	0.7347	0.7702
Ref.[25]	-	0.9106	-	-

Table 2: Normalized moment intensity factor F_I (Symmetric edge crack problem) (b/t=2.0).

d/b	0.2	0.3	0.4	0.5	0.6
Regular model	1.3726	1.1216	0.9884	0.9119	0.8711
Irregular model	1.3719	1.1201	0.9886	0.9110	0.8706
Ref. [46]	1.3689	1.1174	0.9844	0.9086	0.8673

Table 3: Normalized moment intensity factor F_I (Symmetric edge crack problem) (b/t=10.0).

d/b	0.2	0.3	0.4	0.5	0.6
Regular model	1.1158	0.9242	0.8268	0.7719	0.7386
Irregular model	1.1144	0.9225	0.8246	0.7697	0.7377
Ref. [46]	1.1140	0.9250	0.8268	0.7692	0.7351

Nomenclature

Latin symbols

a: crack half length
A_K: area of Ω_K
A_{Ki}: area of Ω_{Ki}
b,c: width and length of the plate
$\boldsymbol{b}(\boldsymbol{x})$: coefficient vector in Eq.(9)
d: distance between crack tips
ds_i: segment for J-integral by nodal integration
$\boldsymbol{d}_i(\boldsymbol{x})$: component vector for deflection and rotations
$\boldsymbol{d}_I$, d_{iI}: coefficient vector of node I
$\mathbf{D}^b$, $\mathbf{D}^s$: matrices in terms of the bending and shear components
E: Young's modulus
$\boldsymbol{f}_I$, $\boldsymbol{f}^p{}_I$: force vector and vector for penalty term
F_1: normalized value of K_1
G: shear modulus
h: a parameter that determines the function support in Eq.(10)
h^p: node spacing of the meshfree models
$\boldsymbol{H}(\boldsymbol{x})$: basis vector in Eq.(9)
K_1: shear force stress intensity factor
$\boldsymbol{K}_{IJ}$, $\boldsymbol{K}^p{}_{IJ}$: stiffness matrix and matrix for penalty term
$\boldsymbol{M}$, M_{ij}: moment
$\boldsymbol{n}$, n_i: normal to the Voronoi cell
$\boldsymbol{N}_I$: matrix composed of the RKs
p: pressure
$\mathbf{Q}$, Q_i: shear force
s: normalized distance from the center of the kernel in Eq.(10)
$s_0(\boldsymbol{x})$, s_1, $s_2(\boldsymbol{x})$: parameters for s in Eq.(30)
t: plate thickness
$\boldsymbol{u}(\boldsymbol{x})$, u_i: plate deformation
$w(\boldsymbol{x})$: deflection
$w_{,i}$: derivatives of $w(\boldsymbol{x})$
W: strain energy
$\boldsymbol{x}$, x_i: position vector

x'_i: local coordinate from the crack tip

z: plate thickness direction

Greek symbols

α: a penalty parameter

$\boldsymbol{\gamma}$, γ_i: shear strain

Γ: boundary of Ω

Γ_c: crack segment

Γ^g: essential boundary

Γ^h: traction boundary

Γ_{Jint}: path for J-integral

Γ_K: boundary of Ω_K

Γ_{Ki}: boundary of Ω_{Ki}

θ_i: rotation angles

$\theta_{i,j}$: derivatives of θ_i

$\boldsymbol{\kappa}$, κ_{ij}: curvature

$\boldsymbol{\Lambda}_I$: matrix of RKs

ν: Poisson's ratio

$\phi_{aI}(\boldsymbol{x})$: original kernel

$\Psi_I(\boldsymbol{x})$: RKs of node I

$\Psi_{I,i}(\boldsymbol{x})$: derivatives $\Psi_I(\boldsymbol{x})$

Ω: analysis domain

Ω_K: domain for K-th Voronoi cell

Ω_{Ki}: domain for a sub-domain of the K-th Voronoi cell